

Northumbria Research Link

Citation: Guerra-Yáñez, Carlos, Guerra, Victor, Jurado-Verdú, Cristo, Rabadán, José, Pérez-Jiménez, Rafael, Ghassemlooy, Fary and Zvánovec, Stanislav (2022) General framework for calculating irradiance distributions of symmetric surface sources. *Optics Express*, 30 (24). pp. 43910-43924. ISSN 1094-4087

Published by: Optical Society of America

URL: <https://doi.org/10.1364/OE.473168> <<https://doi.org/10.1364/OE.473168>>

This version was downloaded from Northumbria Research Link:
<https://nrl.northumbria.ac.uk/id/eprint/50984/>

Northumbria University has developed Northumbria Research Link (NRL) to enable users to access the University's research output. Copyright © and moral rights for items on NRL are retained by the individual author(s) and/or other copyright owners. Single copies of full items can be reproduced, displayed or performed, and given to third parties in any format or medium for personal research or study, educational, or not-for-profit purposes without prior permission or charge, provided the authors, title and full bibliographic details are given, as well as a hyperlink and/or URL to the original metadata page. The content must not be changed in any way. Full items must not be sold commercially in any format or medium without formal permission of the copyright holder. The full policy is available online: <http://nrl.northumbria.ac.uk/policies.html>

This document may differ from the final, published version of the research and has been made available online in accordance with publisher policies. To read and/or cite from the published version of the research, please visit the publisher's website (a subscription may be required.)



General framework for calculating irradiance distributions of symmetric surface sources

CARLOS GUERRA-YÁNEZ,^{1,*}  VICTOR GUERRA,²  CRISTO JURADO-VERDÚ,³  JOSÉ RABADÁN,³ RAFAEL PÉREZ-JIMÉNEZ,³  ZABIH GHASSEMLOOY,⁴  AND STANISLAV ZVÁNOVEC¹ 

¹*Department of Electromagnetic Field, Czech Technical University in Prague, 16627 Prague, Czech Republic*

²*Pi Lighting Sarl, 1950, Sion, Switzerland*

³*Institute for Technological Development and Innovation in Communications, University of Las Palmas de Gran Canaria, 35017 Las Palmas de Gran Canaria, Spain*

⁴*Optical Communications Research Group, Northumbria University, NE1 8ST Newcastle, UK*

*guerrcar@fel.cvut.cz

Abstract: Symmetries in system modeling can be exploited to obtain analytical results on the system behavior and to speed up computations using the symmetric model. This work explores the use of symmetries in radiant surfaces for calculating the induced irradiance distributions by developing a general mathematical expression. The obtained model is applied to flat, cylindrical, and spherical sources to obtain explicit expressions. An experimental evaluation of the flat source is carried out and compared with a traditional point source, and the obtained procedure for the flat scenario is compared with the direct integration approach, which shows an improvement in the computation time of at least two orders of magnitude with a relative root mean square error of less than 10%. The results show that the proposed approach enhances short-range predictions for extended sources. To demonstrate the impact of this in optical wireless communications we have outlined a few applications.

© 2022 Optica Publishing Group under the terms of the [Optica Open Access Publishing Agreement](#)

1. Introduction

The use of symmetries in model analysis is known to yield insightful theoretical results and powerful computation algorithms. Group theory is the framework used to express the symmetries of mathematical models. When an object is described as symmetric, it means that it is invariant under the action of a group of transformations, which is its symmetry group [1]. Deep insights of the model that is being used can be obtained by studying the properties of the symmetry group, i.e., its linear representations [2].

Most of the research work in illumination source characterization focuses on the radiation pattern of point sources. In [3], three different radiation patterns for light emitting diodes (LEDs) were compared in terms of the impulse and frequency responses in an indoor scenario by modelling the multi-path behavior. An analysis of the far-field conditions for the LED radiation was presented in [4], where the far field distance was obtained for different LED chips and optics configurations, as well as a quasi far-field and a minimum-field condition for practical purposes. In [5], the effects of the radiation pattern on the captured power were studied using cosine power-based intensity functions to model the LED sources. The radiation pattern for a bent OLED panel was studied in [6] using a Gaussian mixture model. Note that, the panel was modeled as a point source, i.e., far-field conditions. In [7], a convolutional model for the computation of the irradiance map of LEDs over short distances was presented by I. Moreno. The model derived in his work is a consequence of the symmetrical nature of the scenario being analyzed, and it is derived in the present work as a corollary from the general results for symmetrical exitance distributions. Other results similar in nature are well-known and related

to the radiation transfer for infinite planes, cylinders, spheres, or other symmetrically-shaped radiation sources [8]. Here, we follow this line of thought and we analyze a radiometric problem where the source is contained within a symmetric surface, thus limiting the results to this scenario. It should be noted that this does not imply a tight limitation on its applicability, since many real world scenarios can be characterized with sources embedded within symmetric surfaces.

The main goal of this work is to analyze the conditions under which the irradiance map obtained in a radiometric problem, expressed as the application of an invariant operator on the exitance function of the source, takes a convolution form (i.e., is invariant to a given group of transformations). As an application of this result, we derive explicit formulas for computation under selected scenarios. Following this process, simplified expressions for the calculation of the irradiance are obtained. In addition to the theoretical derivation, an experimental validation of the flat source is carried and the results are compared with Lambertian point source model, which is frequently used in optical wireless communication (OWC) [9]. The computational efficiency of the fast Fourier transform algorithm enables the speedy calculation of irradiance distributions using the proposed convolutional models. To illustrate the potential of the proposed work, the derived expressions can be used to model the behavior of flexible curved surfaces in future wearable devices and mobile phones, or to speed up the computation of coverage maps in OWC considering the behavior of large area sources.

The rest of the paper is structured as follows: Section 2 presents an analysis of the simplifications that can be performed by exploiting the symmetries in the computation of irradiance maps. Section 3 particularizes the analysis of the previous section to the flat, cylindrical, and spherical symmetries. Section 4 presents an experimental validation of the flat scenario analyzed in Section 3, as well as a comparison between the proposed simplifications and the direct calculation of the irradiance. Section 5 outlines a discussion on potential applications of the proposed models in OWC scenarios. Finally, Section 6 concludes this paper.

2. Exploitation of symmetries on irradiance computations

In this section, it is shown that an explicit convolution formula can be obtained for non-coherent radiating surfaces with the symmetry group consisting of direct isometries by using tools from group theory, i.e., linear representations. Figure 1 illustrates the geometry that will be used in this derivation. For the non-coherent light propagating through a non-absorbent media with a homogeneous refractive index, the spectral irradiance at a given point and orientation can be obtained from the spectral radiance function of a source L_λ , which is given by [10]:

$$E_\lambda(\mathbf{r}) = \iint_S L_\lambda(\mathbf{r}', \theta, \phi) \frac{\cos(\theta) \cos(\psi)}{R^2} dS', \quad (1)$$

where λ denotes the wavelength of the considered light. S is the surface in \mathbb{R}^3 where the source is defined. θ and ψ are the angles between the line joining the source with the evaluation point and the normal vectors of the source and the evaluation point, respectively. ϕ is the azimuth angle from the surface of the source, \mathbf{r} and \mathbf{r}' define the evaluation point and a point in the source, respectively, and R is the distance between the source and the evaluation point.

Note that, the total irradiance can be recovered from (1) by integrating along the spectrum. For the sake of simplicity, in this work we will always consider the effects for a single wavelength, and thus, we will omit the λ sub index in the rest of the paper.

Note, the cosine terms can be expressed as [11]:

$$\cos(\psi) = \mathbf{n} \cdot \frac{\mathbf{r}' - \mathbf{r}}{R}, \quad (2)$$

and

$$\cos(\theta) = \mathbf{n}' \cdot \frac{\mathbf{r} - \mathbf{r}'}{R}, \quad (3)$$

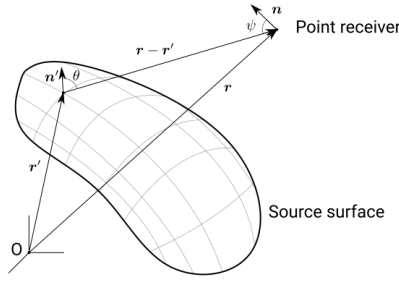


Fig. 1. Geometry of the radiometric problem under analysis. The point O represents the origin of coordinates.

where \mathbf{n} and \mathbf{n}' are the unitary orientation vectors at the evaluation point and each point of the surface, respectively. Note that, \mathbf{n}' is the unitary normal vector to the surface at each point, and it is intrinsically related to the surface geometry. For an extended source with uniform radiation characteristics (i.e., angular behavior), the radiance term can be separated into the exitance function $M(\mathbf{r}')$ and the directivity $D(\theta, \phi)$ at each point of the surface, as given by [10]:

$$L(\mathbf{r}', \theta, \phi) \cos(\theta) = \frac{M(\mathbf{r}') D(\theta, \phi)}{4\pi}. \quad (4)$$

Equation 1 can be rewritten considering 2, 4, and the azimuthal symmetry for $D(\theta, \phi)$, which holds for most of the practical applications using e.g., flat panel organic light emitting diodes (OLEDs), as given by:

$$E(\mathbf{r}) = \iint_S M(\mathbf{r}') \frac{-D(\theta) \mathbf{n} \cdot (\mathbf{r} - \mathbf{r}')}{4\pi R^3} dS'. \quad (5)$$

The calculation of E can be regarded as the action of an operator $T[\cdot]$ on M , which is given by:

$$T[f(\mathbf{r})] = \iint_S f(\mathbf{r}') \frac{-D(\theta) \mathbf{n} \cdot (\mathbf{r} - \mathbf{r}')}{4\pi R^3} dS'. \quad (6)$$

One of the goals of this work is to define conditions under which $T[\cdot]$ can be expressed as a convolution operator, and then derive closed form expressions for the plane, cylindrical and spherical scenarios. This results in a reduced computational complexity by using the fast Fourier transform. Let G be a group of transformations consisting of isometries (i.e., an isometry group) acting on \mathbb{R}^3 . We define the operator $L_g[\cdot]$ for every g in G such that for any function $f(\mathbf{r})$ with its domain on \mathbb{R}^3 the operator is defined by the action of g on the position vector \mathbf{r} , i.e., $L_g[f(\mathbf{r})] = f(g\mathbf{r})$. Here, we are interested in determining under which conditions G induces a family or operators that commute with $T[\cdot]$. The closed form convolution expression follows directly from the commutation of these operators. The following statements outlines the sought conditions and the proof can be found in Appendix 6: if S is G -invariant, i.e., G is the symmetry group of S , then T and L_g commute for all g in G .

The next objective is to express everything as functions of the elements of G . If there is an element \mathbf{r}_0 of S and a subgroup H of G such that the orbit of \mathbf{r}_0 under the action of H spans S and there is a bijective correspondence between the elements of H and the points in S , then we can define M as a function of the elements of H as $M(g, \mathbf{r}_0) = M(g\mathbf{r}_0)$.

Now, if we find another transformation group (not necessarily constituted by isometries), K , such that $H \times K$ spans \mathbb{R}^3 as the orbit of \mathbf{r}_0 , then we can rewrite the evaluation position vector as $\mathbf{r} = gk\mathbf{r}_0$. The next statement will prove useful to demonstrate that $T[\cdot]$ is a convolutional operator and the proof is shown in Appendix 6: the exitance of the source can be expressed as a

linear combination of elementary contributions over the elements of H , which are represented as delta distributions.

The following statement is the main contribution of this work and the proof is shown in Appendix 6: let G be a group of direct isometries (rotations and translations) of \mathbb{R}^3 such that S is invariant under the action of G and for some \mathbf{r}_0 in S there exists a subgroup H of G such that it generates S as the orbit of \mathbf{r}_0 . Then $T[\cdot]$ can be expressed as a convolution operator acting on M with a kernel that depends on the parameters of the source.

3. Analysis of three symmetric scenarios

In this section, the results from the previous section will be particularized for three 2D subgroups of the isometry group of \mathbb{R}^3 , namely: translations in a plane (i.e., plane symmetry), translations and rotations around the same axis (i.e., cylindrical symmetry), and rotations in a sphere (i.e., spherical symmetry). We assume that, for the sake of simplicity, every point of the source has a Lambertian radiation pattern with the directivity defined as:

$$D(\theta) = 2(m + 1) \cos^m(\theta), \quad \theta \in [0, \pi/2], \quad (7)$$

where m is the Lambertian ordinal coefficient of the source, which is assumed to be constant for the source, and for point sources it is estimated as $m = -\ln(2) / \ln(\cos(\theta_{1/2}))$, where $\theta_{1/2}$ is the angle at half irradiance [12]. The steps followed in the analysis are: (i) precise formulation of the problem, including a proper parametrization of the surface; (ii) definition of a position \mathbf{r}_0 and an orientation \mathbf{n}_0 in the surface of the source; (iii) definition of the representation of the symmetry group, G , and choice of H and K ; and (iv) application of the formulas of Appendix 6 to the stated scenario to derive a convolution formula. These convolution expressions can be efficiently implemented using the harmonic analysis techniques (i.e., diagonalization of the convolution kernel) to reduce the computational complexity. The computation would be: 1) decomposition of the exitance function by using the orthogonal basis corresponding to the symmetry group in each case; 2) decomposition of the convolution kernel by using the same basis; 3) multiplication of the two spectra; and 4) recovering the irradiance distribution by inverting of the transform.

3.1. Plane symmetry

The source surface is considered to be a plane with defining equation $z = 0$, for the sake of simplicity, thus being isomorphic to the Euclidean plane, i.e., \mathbb{R}^2 . Therefore, the surface will be represented using the following parametrization in Cartesian coordinates in \mathbb{R}^3 :

$$\mathbf{r}'(x', y') = x' \mathbf{u}_x + y' \mathbf{u}_y. \quad (8)$$

The initial point in the surface is chosen to be $\mathbf{r}_0 = \mathbf{0}$, and the orientation vector of the evaluation point is considered to be facing towards the negative z direction, i.e., $\mathbf{n}_0 = -\mathbf{u}_z$. In this way, the evaluation point is facing the surface directly, considering that the surface radiates to the positive z region.

The symmetry group to consider in this case is a 2-parameter translation group T_{u_x, u_y} with translation vectors parallel to the plane of the source. The action of this group will be represented as a vector addition. Note, for any g in T_{u_x, u_y} , we have:

$$g(x, y) \mathbf{r} = \mathbf{r} + x \mathbf{u}_x + y \mathbf{u}_y. \quad (9)$$

For any point \mathbf{r}_0 in \mathbb{R}^2 , T_{u_x, u_y} is the minimal subgroup of T_{u_x, u_y} that generates \mathbb{R}^2 as an orbit of \mathbf{r}_0 , that is to say, $H = G$ in this case. On the other hand, the K group is considered to consist of translations in the orthogonal direction to the plane, i.e., T_{u_z} . Note, the action of K is defined analogously to G .

The convolution formula for this scenario is:

$$E(x, y, z) = M(x, y) * h_{\text{plane}}(x, y, z), \quad (10)$$

which is a bi-dimensional convolution between the exitance function and a kernel, which is expressed as:

$$h_{\text{plane}} = \frac{(m+1)z^{m+1}}{2\pi(x^2 + y^2 + z^2)^{\frac{m+3}{2}}}. \quad (11)$$

3.2. Cylindrical symmetry

For a cylindrical surface with radius ρ_0 the position vector in cylindrical coordinates is given as:

$$\mathbf{r}'(\phi', z') = \rho_0 \mathbf{u}_\rho(\phi') + z' \mathbf{u}_z. \quad (12)$$

The initial point is considered to be lying on the x axis, and for $\phi = 0$ we have:

$$\mathbf{r}_0 = \rho \mathbf{u}_\rho(0) = \rho \mathbf{u}_x. \quad (13)$$

Note that, the initial orientation vector of the evaluation point is considered to be facing towards the closest point in the source, i.e., the negative x direction, and it is given as:

$$\mathbf{n}_0 = -\mathbf{u}_\rho(0) = -\mathbf{u}_x. \quad (14)$$

The symmetry group for the cylindrical scenario is isomorphic to the direct product of the translation (T_{u_z}) and rotation (SO(2)) groups around the z axis, i.e., $T_{u_z} \times \text{SO}(2)$ and, as in the previous scenario, it is isomorphic to the surface that we are working with. The action of any element g of the symmetry group is represented as an affine transformation given by:

$$g(\phi, z) \mathbf{r} = R_z(\phi) \mathbf{r} + z \mathbf{u}_z, \quad (15)$$

where $R_z(\phi)$ is a rotation matrix given by:

$$R_z(\phi) = \begin{pmatrix} \cos(\phi) & -\sin(\phi) & 0 \\ \sin(\phi) & \cos(\phi) & 0 \\ 0 & 0 & 1 \end{pmatrix}. \quad (16)$$

The subgroup H is in this case the whole G , as in the previous case, and the K group could be chosen to be the multiplication by a non-negative scalar factor in the radial direction.

The following convolution formula can be obtained for the irradiance map:

$$E(\rho, \phi, z) = M(\phi, z) * h_{\text{cylinder}}(\rho, \phi, z), \quad (17)$$

which defines the composition between a linear convolution along the z axis and a circular convolution on the ϕ coordinate. The kernel for this case is given by:

$$h_{\text{cylinder}} = \frac{\rho_0 (m+1) [\rho - \rho_0 \cos(\phi)] [\rho \cos(\phi) - \rho_0]^m}{2\pi(\rho_0^2 + \rho^2 - 2\rho_0\rho \cos(\phi) + z^2)^{\frac{m+3}{2}}} \quad (18)$$

for ϕ in $(-\phi_C, \phi_C)$, with $\phi_C = \arccos(\rho_0/\rho)$, and zero otherwise.

3.3. Spherical symmetry

For a spherical surface of radius R_0 , the parametrization used is given in spherical coordinates as:

$$\mathbf{r}_S = R_0 \mathbf{u}_R(\theta', \phi'). \quad (19)$$

The initial evaluation point is considered to be lying on the north pole of the sphere (positive z -axis), i.e., $\theta' = \phi' = 0$, and is given by:

$$\mathbf{r}_0 = R_0 \mathbf{u}_R(0, 0) = R_0 \mathbf{u}_z. \quad (20)$$

Note that, the orientation vector is considered to be facing towards the radial direction, i.e., towards the spherical source, and is given as:

$$\mathbf{n}_0 = -\mathbf{u}_R(0, 0) = -\mathbf{u}_z. \quad (21)$$

The symmetry group in the spherical scenario is the 3D rotation group, i.e., $SO(3)$, which is non-abelian, in contrast to the previous groups. This group describes rotations in the 3D space and it is not isomorphic to the sphere, which makes a more careful analysis necessary.

The action of any element of the symmetry group is represented by a linear operator (a rotation matrix) over the points in space described as position vectors, which can be decomposed into three rotations by using the proper Euler angles [13] as given by:

$$g(\alpha, \beta, \gamma) \mathbf{r} = R_z(\alpha) R_y(\beta) R_z(\gamma) \mathbf{r}, \quad (22)$$

where α , β , and γ denote the proper Euler angles for rotations around the z axis, then y axis, then z axis again. The sphere can be recovered as the orbit of \mathbf{r}_0 by considering the subgroup formed by rotations over the y axis, limiting β to the $[0, \pi]$ range, followed by rotations over the z axis, i.e., $\gamma = 0$. The group K is considered to be multiplication by a non-negative scalar of the position vectors.

A convolution formula can be derived with the conditions defined by the spherical symmetry. As G is non-abelian in the spherical case, the convolution is non-commutative. However, the kernel of the convolution is invariant to the action of rotations $R_z(\omega)$ in the proper Euler angle decomposition. If the surface is parameterized using the Euler angles as discussed previously, then the recovered convolution is commutative, and it is given by:

$$E(R, \theta, \phi) = M(\theta, \phi) * h_{\text{sphere}}(R, \theta, \phi), \quad (23)$$

where the $*$ operation is a spherical convolution (i.e., rotations cannot be identified with additions in this scenario, as 3D rotations define a non-abelian group). Note that, the kernel of the convolution presents azimuthal symmetry. This can be shown by calculating the kernel in terms of θ' and ϕ' for the points in the z -axis in the particularization of (38) for this case, and we obtain:

$$h_{\text{sphere}}(\text{id}, R/R_0, \mathbf{r}_0) = \frac{R_0 \sin(\theta') (m+1) [R \cos(\theta') - R_0]^m [R - R_0 \cos(\theta')]}{2\pi [R^2 + R_0^2 - 2RR_0 \cos(\theta')]^{\frac{m+3}{2}}} \quad (24)$$

for θ in $(0, \theta_C)$, with $\theta_C = \arccos(R_0/R)$, and zero otherwise.

The azimuthal symmetry is explicit in this expression (i.e., the kernel does not depend on ϕ'). This symmetry further simplifies the computation of the irradiance map because only the coefficients for Y_l^0 need to be considered in the spectral decomposition of the kernel [14]. Note that, even though the spherical convolution involves rotation operations, it can be diagonalized by computing the spherical harmonic decomposition of the exitance distribution and the convolution kernel. The spherical harmonic decomposition can be efficiently evaluated using the fast Fourier transform [15].

4. Experimental evaluation of the flat case

An experimental evaluation of the derived model for the case of a flat source is performed using a Huawei P9 smartphone LCD screen and a photodiode attached to the mechanical positioning system of a 3D printer. The setup used is illustrated in Fig. 2. The optical source is a 1080×1920 pixel array with an area of $\sim 69 \text{ cm}^2$, as shown in Fig. 2(b). The optical power was measured using a Si photodiode (Thorlabs PDA36A), with an active area $A_{Rx} = 13 \text{ mm}^2$, connected to an oscilloscope (MSO7034A) and attached to the header of a 3D printer, as observed in Fig. 2(d). The angle of view (AoV) of the receiver (Rx) was controlled using plastic occluders. The occluders for particular AoV were designed using a cylindrical structure that can be appreciated in Fig. 2(c). The measurements were performed with the photodiode pointing downwards directly facing the source plane. A picture of the experiment under execution is shown in Fig. 2(a). The sampling distance needed for an adequate measurement procedure was determined by obtaining the irradiance distributions for the different scenarios using direct integration, and then obtaining the Fourier transform from the distribution. A sampling distance of $\Delta x = \Delta y = 5 \text{ mm}$ was enough to recover the original distribution from the sampled points without significant aliasing under the worst scenario. The sampling area was a $19 \times 19 \text{ cm}^2$ square, which leads to the use of a 39×39 spatial grid for sampling. The Rx was moving along a meander path and the captured power was measured at each position of the spatial grid. The center of the spatial grid is aligned with the center of the source. This process was repeated for each AoV at 6 different distances from the source plane. As for the modeling of the AoV limitation, it can be done by multiplying the kernel by a factor in 38, which models the dependence on the incidence angle ψ at the Rx. In this case, a rectangular window was used to model the effect of the occluder, although the use of more precise models might be considered in future works. The simulation was performed using the proposed convolution scheme and direct integration using a quadrature rule for comparison purposes. The results of the simulations, measurements, and Lambertian point source model are compared using the maximum value of the zero-normalized cross correlation (ZNCC) and the behavior of the irradiance maps is discussed for some particular AoV values and distances. Table 1 summarizes the most important experiment and simulation parameters used in this work.

Table 1. Experiment and simulation parameters

Source array	$1920 \times 1080 \text{ px}$
A_{Source}	$\sim 69 \text{ cm}^2$
m	3.5
Sampling grid	39×39
Δx	0.5cm
Δy	0.5cm
A_{Rx}	13 mm^2
G_{Rx}	$4.75 \cdot 10^3 \text{ V/A}$
AoV	$\{13.78, 23.53, 41.12\}^\circ$

The ZNCC can be expressed as [16]:

$$\text{ZNCC}(X_{i,j}, Y_{i,j}) = \frac{\sum_i \sum_j (X_{i,j} - \bar{X})(Y_{i,j} - \bar{Y})}{N\sigma_X\sigma_Y} \quad (25)$$

where $X_{i,j}$ and $Y_{i,j}$ denote two bi-dimensional signals, whose average values and standard deviations are denoted by \bar{X} , \bar{Y} , and σ_X , σ_Y , respectively, and N denotes the total number of samples.

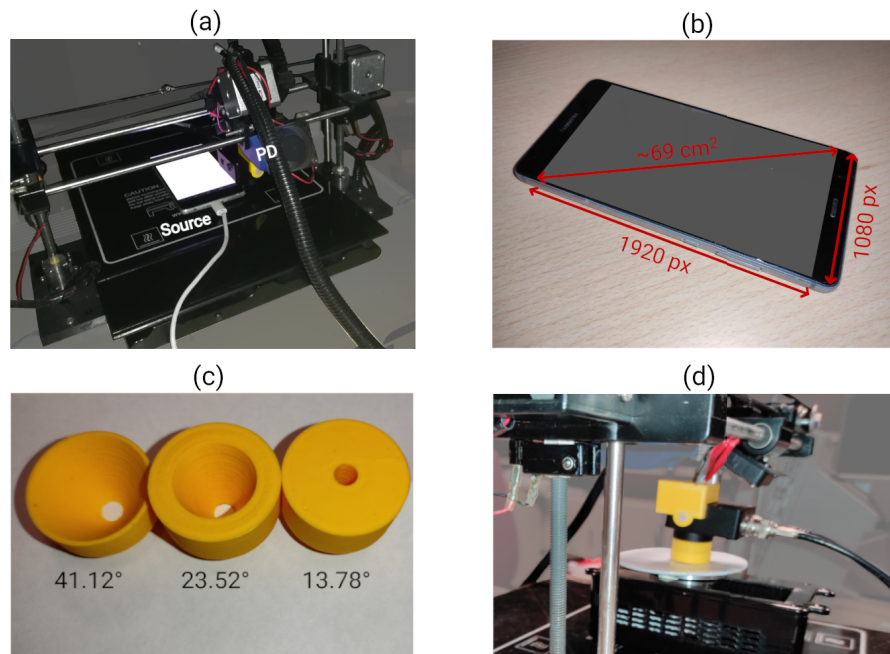


Fig. 2. Pictures of the experimental setup used for the evaluation of the flat scenario. (a) Experiment under execution; (b) smartphone screen source; (c) occluders used for 41.12° , 23.52° , and 13.78° AoV limitation; and (d) a different angle where the occluder can be seen coupled to the PD.

Figure 3 shows the maximum value of the ZNCC of the experimental data for a range of AoV values with: the derived convolutional model represented with solid lines; and the Lambertian point source model shown in dashed lines. The results show that the Lambertian point source model offers improved accuracy with the increasing distance from the source and the Rx's AoV, while the convolutional model matches the experimental data with a $\text{ZNCC} > 0.98$ for all cases analyzed. Therefore, this graph shows that the point source model should only be used when the dimensions of the source are negligible compared to the link span. Note, the validity of the point source model for different source geometries will be further investigated in future works.

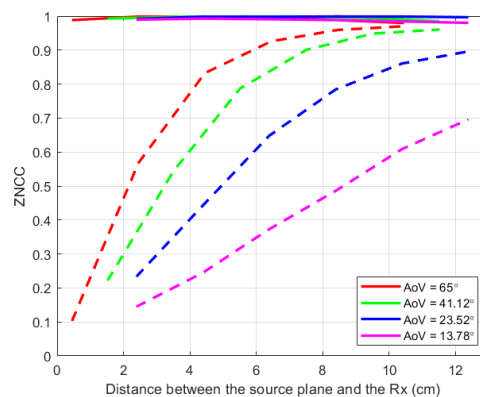


Fig. 3. ZNCC comparing the experimental data with the convolutional model (solid lines) and the Lambertian point source model (dashed lines).

Figures 4–6(a) and (b) show the measured and simulated captured optical power profiles for the proposed system shown in Fig. 2 for AoV 13.78° , 23.52° , and 65° , at a distance of 8.4 cm from the source plane, whereas the measured and simulated power profiles of vertical and a horizontal sections are depicted in Figs. 4, 5(c) and (d). Also shown are the plots for the predicted profile using the Lambertian point source approximation with the same transmit power for the point source positioned at the center of the surface. Note that, the captured power levels of the suggested model are noticeably different to the predicted plots for the Lambertian point source model for smaller values of AoV. This is because for the point source scenario the Rx either captures power from the source or does not capture anything at all, whereas for the extended source case the power of the source is distributed along its surface, thus the Rx can capture power from the source in some regions with no received signal from the point source model (see Fig. 5(c) for a clear illustration). Note, for other cases only a fraction of the source power will reach the Rx, thus the predicted data for the convolutional model is lower than for the Lambertian point source model (see Fig. 4(c)). Similar behavior has been reported in [7] with the following differences: (i) LED chips with smaller surface areas were used; (ii) link ranges of up to a few millimeters; (iii) an image sensor-based Rx; and (iv) not considering the effects of the AoV.

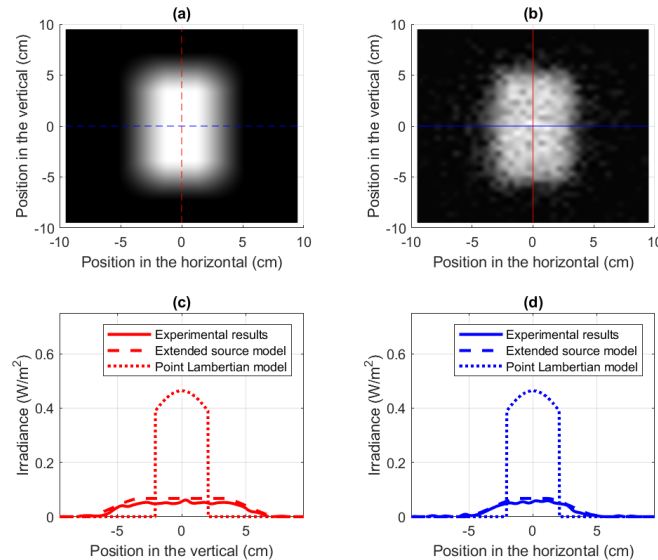


Fig. 4. Simulated (a) and experimental (b) irradiance maps using an AoV of 13.78° at a distance of 8.4 cm. A profile of the vertical (c) and horizontal (d) section is shown.

Figure 7(a) shows the computation time of the convolution-based approach against the direct computation of the integral using a 2.6 GHz CPU. Considering an $N \times N$ grid for the computation of the irradiance map, the computational complexity of the direct integration method is $O(N^4)$, while for the proposed convolutional method implemented using the fast Fourier transform it is $O(N^2 \log(N^2))$ [17]. Therefore, the measured computation time is several orders of magnitude lower for the proposed method compared to the direct computation. The relative root mean square error (RRMSE) between the convolutional model and the direct computation for the same grid sizes is presented in Fig. 7(b).

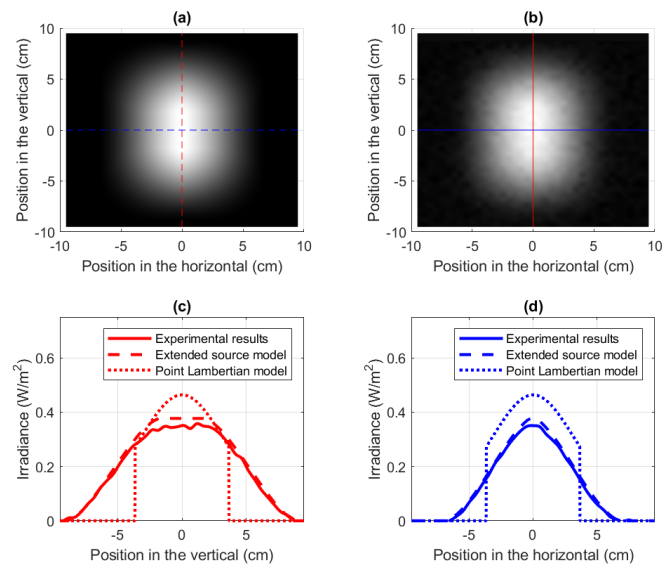


Fig. 5. Simulated (a) and experimental (b) irradiance maps using an AoV of 23.52° at a distance of 8.4 cm. A profile of the vertical (c) and horizontal (d) section is shown.

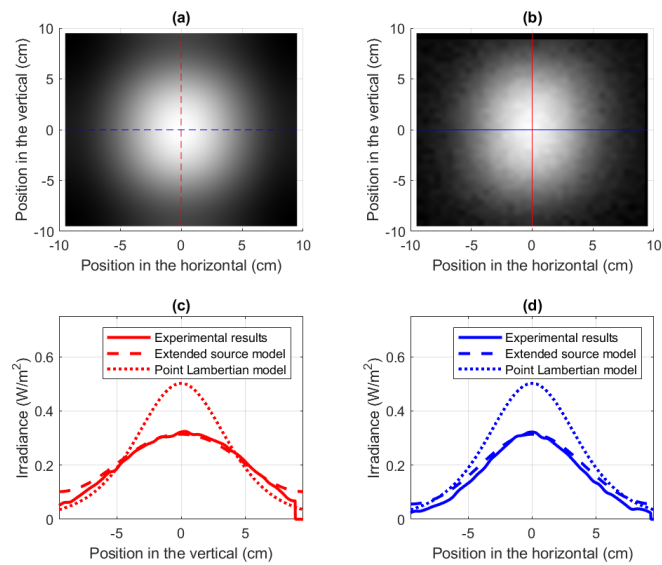


Fig. 6. Simulated (a) and experimental (b) irradiance maps without occluder (AoV of 65°) imposed by the geometry of the PD at a distance of 8.4 cm. A profile of the vertical (c) and horizontal (d) section is shown.

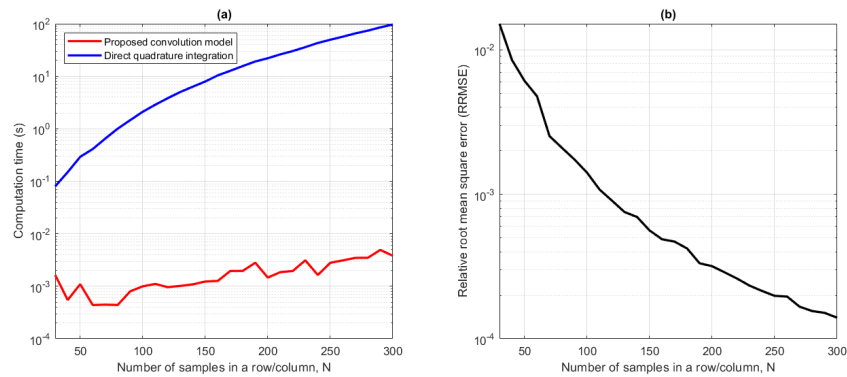


Fig. 7. Performance comparison between the proposed convolutional model (red) and the direct computation (blue) of the irradiance distribution. The performance was evaluated using the computation time of the irradiance map at 1.5 m with an AoV of 15° against grid size, shown in (a), and the relative root mean square error, shown in (b).

5. Application in optical wireless communication (OWC)

The conditions stated in Section 3 for the plane and cylindrical scenarios are met in the following example application in OWC. Here, we consider the case of line-of-sight modeling of flat sources for the link budget and interference analysis. The figures of this section illustrate the power of the proposed framework by using the expressions from Section 3.1 for the plane scenario.

The received power determines the performance of the communication system, among other parameters, which can be estimated from the irradiance map as $P_{Rx} \approx EA_{Rx}$, where A_{Rx} is the active area of the photo-detector, which must be several orders of magnitude lower than any other geometrical parameter to apply the point Rx approximation. In addition, optical elements are often included in the Rx design to limit the AoV. In that case, the integrand of (1) should be modified by including a factor that models the behavior of the optical system as a function of ψ , as in Section 4. Note, all conditions stated in Section 2 still hold, and the derived convolution formulas with some modifications can still be applied.

To illustrate this application, in Fig. 8, a rectangular array of illumination sources is shown, where each source is $10 \times 40 \text{ cm}^2$, and the separation between the centers of two neighbouring sources is 1 m. The source positioned at the center of the distribution is acting as a Tx, whereas the sources shown in red are introducing interference. We have considered a total transmit power of 1 W per source, an Rx with an active area of 1 cm^2 , and the noise power considered is $0.1 \mu\text{W}$. The computations were performed at a distance of 1.5 m from the source plane, and for the AoV values of 15° and 30° , the irradiance maps are shown in Figs. 9(a) and (b), while the distributions of the signal-to-noise ratio (SNR) and signal-to-interference and noise ratio (SINR) are depicted in Figs. 9(c) and (d), and (e) and (f), respectively. The power collected from the primary source, shown in blue in Fig. 8, is the signal, while the power caught from the secondary sources, shown in red in Fig. 8, is the interference. These two powers are used to calculate the SINR.

These maps show that, even though the received power (i.e., irradiance) increases with AoV, the SINR might be impaired because of the higher levels of interference. This example illustrated how the proposed model could be used for the analysis of practical scenarios when designing an OWC system. It is necessary, however, to conduct a parallel experimental evaluation of this to validate the use of this method in OWC applications and to derive significant conclusions.

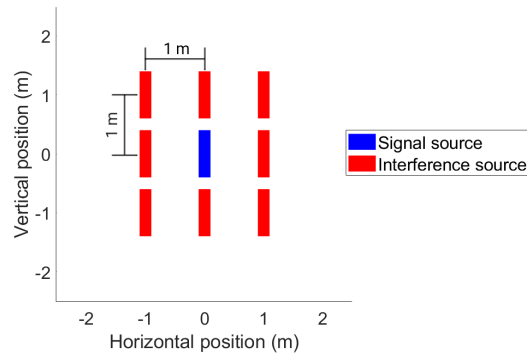


Fig. 8. Exitance of the analyzed source distribution. The red surface corresponds to the surface transmitting the desired signal, while the blue ones represent the interference signals.

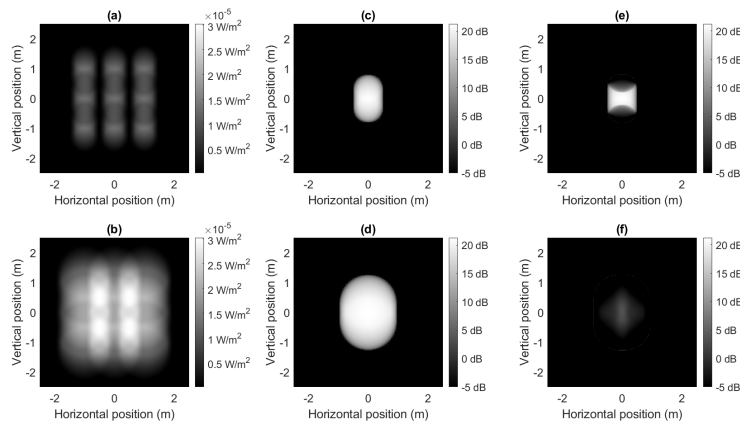


Fig. 9. Illustration of: the irradiance map calculated for the whole array of sources, see (a) and (b); the interference-free SNR distribution, see (c) and (d); and the SINR map considering the center source to be transmitting information and the other sources to be interfering, see (e) and (f). The computations were performed considering an AoV of 15° , for (a) and (c), and 30° , for (b) and (d).

6. Conclusion

In this work, we have investigated the effects of considering symmetries in the computation of irradiance maps using the fundamentals of radiometry as well as the tools from group theory and representation theory. The main result of this work was the derivation of a general convolution formula for strictly symmetric scenarios, which was particularized for the flat, cylindrical, and spherical scenarios under additional conditions (Lambertian sources fixed orientation of the detector towards the source). Convolution expressions were derived, and an explicit formula for the kernels was given for each one of these cases. In addition, an experimental evaluation of the flat scenario was performed, and the results were compared to the Lambertian point source model, which is frequently used in OWC system design. The results showed that, if the dimensions of the source are in the same order of magnitude as the link span, the point source model is not able to predict two important aspects of the captured power maps, namely: (i) the shape of the map and (ii) the actual captured power level. As well, we compared the proposed convolutional method with the direct integration approach, showing a significant reduction in

the computation time, at least two orders of magnitude, with an RRMSE lower than 10% for all grid sizes. This work presented a preliminary examination of the effects of not considering the surface nature of extended sources in the link budget analysis of OWC systems. A thorough analysis of these effects and their consideration in OWC system design will be the object of future research. The proposed convolutional model can improve the estimation of the received power for LOS link design when extended sources are being used, such as in [18]. A discussion of the possible application scenarios in OWC of the convolutional model was also presented, proving the potential impact that considering the surface nature of sources might have in the future design of short and medium-range OWC links in the future. The experimental evaluation of the cylindrical and spherical symmetry models will be performed as future work. We will consider extending the current framework to asymmetrical sources, which can be decomposed into locally symmetric sources. Other research directions following the current work include the development and testing of the scheme presented in Section 5, assessing the user mobility and illumination-communication coexistence in VLC-enabled femto-cells for 5G and beyond, and other applications based on the behavior of the extended sources, including positioning, multiple access schemes exploiting the spatial separation of the different channels for the different analyzed geometries.

Appendix A

This appendix contains a proof of the commutativity of the irradiance operator when the surface is G -invariant.

The proof is straightforward. We begin by successively applying L_g and T to M as follows:

$$T[L_g[M(\mathbf{r})]] = \iint_S M(g\mathbf{r}') \frac{-D(\theta) \mathbf{n} \cdot (\mathbf{r} - \mathbf{r}')}{4\pi R^3} dS'. \quad (26)$$

Substituting $g\mathbf{r}' = \mathbf{r}''$ (which also yields $g\mathbf{n}' = \mathbf{n}''$) in the last integral of (26) we obtain:

$$\iint_S M(\mathbf{r}'') \frac{-D(\theta) \mathbf{n} \cdot (\mathbf{r} - g^{-1}\mathbf{r}'')}{4\pi R^3} dS'', \quad (27)$$

where θ and R are given by:

$$\theta = \arccos\left(g^{-1}\mathbf{n}'' \cdot \frac{\mathbf{r} - g^{-1}\mathbf{r}''}{R}\right) \quad (28)$$

and

$$R = \|\mathbf{r} - g^{-1}\mathbf{r}''\|, \quad (29)$$

respectively, and $dS'' = dS'$ because the first fundamental form is invariant under the action of isometries [19].

Now, as any g in G preserves the internal product and the metric, (27) can be written, after the action of g , as:

$$\iint_S M(\mathbf{r}'') \frac{-D(\theta) g\mathbf{n} \cdot (g\mathbf{r} - \mathbf{r}'')}{4\pi R^3} dS'', \quad (30)$$

and θ and R can be expressed as:

$$\theta = \arccos\left(\mathbf{n}'' \cdot \frac{g\mathbf{r} - \mathbf{r}''}{R}\right) \quad (31)$$

and

$$R = \|g\mathbf{r} - \mathbf{r}''\|. \quad (32)$$

Thus, we can rewrite (30) as:

$$\iint_S M(\mathbf{r}'') \frac{-D(\theta) \mathbf{g}\mathbf{n} \cdot (\mathbf{g}\mathbf{r} - \mathbf{r}'')}{4\pi R^3} dS'' = L_g[T[M(\mathbf{r})]]. \quad (33)$$

Note that, when applying the affine transformation, which is a linear mapping that preserves parallelism relations, to the orientation vectors, \mathbf{n} and \mathbf{n}' , only the linear part of the transformation needs to be considered, as they are free vectors. In fact, this applies to the orientation vector of the surface since S is invariant under the action of G [20].

Appendix B

This appendix contains a proof of the linear decomposition of an exitance function using the elements of the invariance group G .

We will begin by expressing the exitance as a linear combination of delta distributions in the coordinate space. The expression obtained is given by:

$$M(\mathbf{r}') = \iint_S M(\mathbf{r}'') \delta(\mathbf{r}' - \mathbf{r}'') dS'. \quad (34)$$

Any position vector in S can be expressed as $\mathbf{r} = g\mathbf{r}_0$ for some given g and \mathbf{r}_0 in H and \mathbb{R}^3 , respectively. Expressing the dummy variable \mathbf{r}'' in (34) in terms of g , the integration can be performed over H given an appropriate Haar measure is defined considering the scaling factor of the area differential [21], and thus, the exitance can be expressed as:

$$M(\mathbf{r}') = \int_H M(g\mathbf{r}_0) \delta(\mathbf{r}' - g\mathbf{r}_0) dg, \quad (35)$$

which is the linear combination that we were looking for.

Appendix C

In this appendix, it is proven that the irradiance distribution can be calculated as a convolution when the surface is G -invariant.

To prove that E can be calculated as a convolution, it must be proven that the $T[\cdot]$ operator is linear, which is trivially true because it is an integral operator, and that it is invariant under the action of G , which was proven in Appendix A. Now, using \mathbf{r}_0 and the associated subgroup H , we can write M in (5) as a linear combination of functions with domain in H as shown in Appendix B:

$$\begin{aligned} & \iint_S \left[\int_H M(l\mathbf{r}_0) \delta(\mathbf{r}' - l\mathbf{r}_0) dl \right] \frac{-D(\theta) \mathbf{n} \cdot (\mathbf{r} - \mathbf{r}')}{4\pi \|\mathbf{r} - \mathbf{r}'\|^3} dS' \\ &= \int_H M(l\mathbf{r}_0) \frac{-D\left(\mathbf{n}'(l\mathbf{r}_0) \cdot \frac{\mathbf{r} - l\mathbf{r}_0}{\|\mathbf{r} - l\mathbf{r}_0\|}\right) \mathbf{n} \cdot (\mathbf{r} - l\mathbf{r}_0)}{4\pi \|\mathbf{r} - l\mathbf{r}_0\|^3} dl. \end{aligned} \quad (36)$$

If the evaluation position vector is expressed as $\mathbf{r} = gk\mathbf{r}_0$ in 36, we get:

$$E(g, k, \mathbf{r}_0) = \int_H M(l, \mathbf{r}_0) h(gl^{-1}, k, \mathbf{r}_0) dl, \quad (37)$$

where we have defined the 2nd function in (37) as:

$$h(g, k, \mathbf{r}_0) = \frac{-D\left(\mathbf{n}'(\mathbf{r}_0) \cdot \frac{gk\mathbf{r}_0 - \mathbf{r}_0}{\|gk\mathbf{r}_0 - \mathbf{r}_0\|}\right) \mathbf{g}\mathbf{n}_0 \cdot (gk\mathbf{r}_0 - \mathbf{r}_0)}{4\pi \|gk\mathbf{r}_0 - \mathbf{r}_0\|^3}. \quad (38)$$

This proves that the operator $T[\cdot]$ is a convolution operator, with a kernel given by $h(g, k, \mathbf{r}_0)$.

Funding. European Cooperation in Science and Technology (CA19111); Agencia Estatal de Investigación (PID2020-114561RB-I00); České Vysoké Učení Technické v Praze (SGS20/166/OHK3/3T/13).

Disclosures. The authors declare no conflicts of interest.

Data availability. Data underlying the results presented in this paper are not publicly available at this time but may be obtained from the authors upon reasonable request.

References

1. W.-K. Tung, *Group Theory in Physics*, vol. 1 (World Scientific, 1985).
2. E. Noether, "Invariante variationsprobleme, math-phys," *Klasse* **1918**, 235–257 (1918).
3. J. Ding, I. Chih-Lin, and Z. Xu, "Indoor optical wireless channel characteristics with distinct source radiation patterns," *IEEE Photonics J.* **8**(1), 1–15 (2016).
4. C.-C. Sun, W.-T. Chien, I. Moreno, C.-C. Hsieh, and Y.-C. Lo, "Analysis of the far-field region of leds," *Opt. Express* **17**(16), 13918–13927 (2009).
5. Y. Wang, M. Chen, J.-Y. Wang, J. Shi, Z. Yang, Y. Pan, and R. Guan, "Impact of led transmitters' radiation pattern on received power distribution in a generalized indoor vlc system," *Opt. Express* **25**(19), 22805–22819 (2017).
6. H. Chen and Z. Xu, "Oled panel radiation pattern and its impact on vlc channel characteristics," *IEEE Photonics J.* **10**(2), 1–10 (2018).
7. I. Moreno and P. X. Viveros-Méndez, "Modeling the irradiation pattern of leds at short distances," *Opt. Express* **29**(5), 6845–6853 (2021).
8. J. Chaves, *Introduction to Nonimaging Optics* (CRC Press, 2008).
9. Z. Ghassemlooy, W. Popoola, and S. Rajbhandari, *Optical Wireless Communications: System and Channel Modelling with Matlab®* (CRC Press, 2019).
10. M. Strojnik and M. K. Scholl, "Radiometry," in *Advanced Optical Instruments and Techniques* (CRC Press, 2017), pp. 459–516.
11. S. Lang, *Introduction to Linear Algebra* (Springer Science & Business Media, 2012).
12. Z. Ghassemlooy, L. N. Alves, S. Zvanovec, and M.-A. Khalighi, *Visible Light Communications: Theory and Applications* (CRC Press, 2017).
13. S. L. Altmann, *Rotations, Quaternions, and Double Groups* (Courier Corporation, 2005).
14. L. Mak, S. Grandison, and R. J. Morris, "An extension of spherical harmonics to region-based rotationally invariant descriptors for molecular shape description and comparison," *J. Mol. Graph. Model.* **26**(7), 1035–1045 (2008).
15. G. A. Dilts, "Computation of spherical harmonic expansion coefficients via fft's," *J. Comput. Phys.* **57**(3), 439–453 (1985).
16. J. R. Parker, *Algorithms for Image Processing and Computer Vision* (John Wiley & Sons, 2010).
17. A. V. Oppenheim, *Discrete-time Signal Processing* (Pearson Education India, 1999).
18. Z. Nazari Chaleshtori, Z. Ghassemlooy, H. B. Eldeeb, M. Uysal, and S. Zvanovec, "Utilization of an oled-based vlc system in office, corridor, and semi-open corridor environments," *Sensors* **20**(23), 6869 (2020).
19. S. Kobayashi and K. Nomizu, *Foundations of Differential Geometry*, vol. 1 (Interscience Publishers, 1963).
20. M. K. Bennett, *Affine and Projective Geometry* (John Wiley & Sons, 2011).
21. J. Diestel and A. Spalsbury, *The Joys of Haar Measure* (American Mathematical Soc., 2014).